Experimental and numerical studies on flexural behaviour of lightweight and sustainable precast fibre reinforced hollow core slabs

Sumit Sahoo, Chetharajupalli Veerendar, S. Suriya Prakash [*]

Department of Civil Engineering, Indian Institute of Technology Hyderabad, Sangareddy, 502285, India

ARTICLE INFO

ABSTRACT

This study reports experimental and numerical studies on the flexural behaviour of sustainable fibre reinforced lightweight hollow core slabs (FR-LWHCS). An innovative and sustainable LWHCS is proposed for structural applications using a lightweight concrete mix of 1800 kg/m^3 density, previously developed by authors. Full-scale precast LWHCS specimens are cast and tested under flexure using a four-point loading configuration. A high shear span to depth (a/d) ratio of 10 is chosen to have flexure dominant behavior. FR-LWHCS is made using sintered fly ash aggregate (SFA) as coarse aggregate and monofilament macro synthetic fibres of different volumetric fibre dosages (0.4 % and 0.6 %). A small dosage of micro synthetic fibres of 0.02 % by volume is also added to arrest shrinkage cracks. Two control slabs, one constructed with lightweight concrete and the other with conventional normal density concrete, are tested. The digital image correlation (DIC) technique is used to track the cracks and failure modes. A 3D finite element analysis is performed to supplement the test results. Test results show that FR-LWHCS satisfies all the structural requirements, leading to economy and sustainability. FR-LWHCS with 0.6 % fibre dosage performed better than hollow core slabs made of normal density concrete. Though the addition of fibres did not considerably increase peak load, a minimum dosage of fibre addition is warranted in LWHCS to improve the serviceability performance. Fibre addition significantly improved the strain energy absorption.

1. Introduction

Structural lightweight aggregate concrete (SLWAC) can replace normal density concrete in certain applications to reduce the structure's dead load without compromising the structural performance requirements. Lightweight aggregate concrete (LWAC) can reduce material and transportation costs, leading to faster construction and superior durability [1,2]. Currently, sintered fly ash aggregate (SFA) is widely used as a manufactured lightweight aggregate due to its excellent mechanical and durability properties [3]. Fly ash, a by-product of coal, is used to produce SFA by the sintering process. Using SFA in construction leads to the sustainable utilisation of fly ash which is otherwise considered waste material. The use of SFA in concrete can reduce its density and make them more eco-friendly [4]. SFA are porous, which permits ingress of cement paste into its voids and makes a better bond with it, thus making concrete strong and durable [5].

Though LWAC has been increasingly used, a few challenges are associated with its usage. LWAC can exhibit higher brittleness if not appropriately designed than normal density concrete due to crack propagation through the lightweight aggregate. In addition, LWAC has lower tensile strength than natural coarse aggregate concrete [6]. However, the drawbacks of the LWAC can be minimized by incorporating fibres in concrete which help in increasing their ductility [7,8]. Steel, synthetic, carbon, glass, and basalt fibres are a few of the widely used fibres in producing fibrous concrete. Synthetic fibres have several advantages due to their resistance to corrosion, chemical stability, and good post-cracking behaviour. Moreover, synthetic fibres are more economical and easy to handle than steel fibres [9–11]. Adding macro and micro synthetic fibres helps arrest cracks at different scales (micro shrinkage and large structural cracks). The synergistic action offered by concrete reinforced with the fibres of different scales (micro and macro) can significantly enhance the performance of concrete [12,13].

Hollow core slabs (HCS) are widely used precast structural components. They have voids running throughout their length. HCS can be used in structural applications in various ways, such as floor elements, load-bearing and non-load-bearing panels, spandrel members and bridge deck units [14]. HCS have various advantages such as economical, faster rate of construction, excellent fire resistance, adequate load

---

capacity, significant flexural rigidity, and excellent thermal and acoustic insulation [15,16]. HCS is a lighter element than the solid slab, and the weight of the HCS can be further reduced by using lightweight aggregate instead of natural coarse aggregate. Many researchers have recently studied the structural behaviour of HCS made of conventional concrete [17–19]. However, only limited work has focussed on lightweight hollow core slabs (LWHCS) [14,20–22]. Previously, researchers examined the performance of HCS using PVC pipes and Styrofoam to create hollow cores in the system [23]. Previous work has shown that incorporating steel and synthetic fibres increases the ultimate failure loads, stiffness and delayed crack propagation in HCS [24]. Failure modes of LWHCS can be different from normal density HCS. Hence, fibres can play a significant role in structural performance improvement. However, the beneficial effects of fibres in load resistance and change in the failure mode of LWHCS have not been explored yet.

Several researchers in the past have examined the flexural behaviour of HCS made of normal density concrete [17,23,25]. The shear span to depth (a/d) ratio significantly impacts the capacity and failure modes of slabs and beams. According to Kani's [26] classical theory, a/d ratio of 6 is the transition point above which reinforced concrete beams can fail in a flexure critical mode. Failure owing to abrupt diagonal shear tension after flexural crack (flexure-shear mode) is expected for a/d ratios between 2.5 and 6. The specimens tested at a/d ratio below 2.5 fail in shear critical mode. Previously presented a/d ratios, however, are only applicable for reinforced concrete beams [27] and not for HCS. In HCS, the a/d ratio and the depth have a dominant influence on their behaviour. Several researchers have previously investigated the effectiveness of fibers in prestressed hollow core slabs [28–31] Also, fibre effects are more pronounced in specimens with a high a/d ratio than in a low a/d ratio [24]. Naser et al. [17] studied flexural behaviour of steel fibre reinforced ferro-cement HCS with embedded polyvinyl chloride (PVC) pipe. The researchers have also observed that HCS exhibited better load–deflection characteristics in terms of ductility and serviceability than solid slabs [15]. Few researchers have found that HCS have the same flexural capacity as solid slabs [23]. Also, some attempts have been made to study the structural behaviour of HCS using finite element analysis [32,33]. The effect of different shapes of the hollow cores, such as spherical, elliptical and mushroom [15], on the behaviour of slabs, was explored. Though several studies exist on HCS, most of them are limited to understanding the flexural behaviour of HCS made with normal density concrete [34–39].

2. Research significance

Numerous studies in the past have focused on the flexural behaviour of HCS made of normal density concrete. However, the available research related to LWAC-based structural components is very minimal. A rational understanding of the behaviour of FR-LWHCS is essential for promoting it as a sustainable structural solution for floor slab applications. Hence, this research aims to understand the flexural response of FR-LWHCS with a density of 1800 kg/m³ through extensive experimental and numerical investigation. The objectives and scope of this study are as follows:

- To study the influence of reduction in density by using SFA and assessing lightweight hollow cores slabs made with SFA for structural applications.
- To understand the flexural behaviour of FR-LWHCS concerning strength, cracking, failure modes, strain energy absorption and serviceability by full-scale tests.
- To examine the effect of synthetic fibres on the performance of lightweight HCS in terms of crack propagation and post-cracking behaviour using full-field strain measurements with the help of the DIC technique.
- To understand the flexural response of FR-LWHCS, using a finite element analysis after careful validation with obtained test results.

Fig. 1. Sintered Fly Ash Aggregate.

3. Experimental program

3.1. Material properties and mix design

A low slump and lightweight concrete of 1800 kg/m³ density were developed to manufacture precast hollow core slab elements. Only salient features of the concrete mix are presented here for completeness and to maintain brevity. More details on the mix design and detailed material characterisation can be found in the companion papers of the authors [3,6]. The lightweight concrete mix design approach was based on volume mix proportions. A nominal quantity of Ordinary Portland Cement (OPC-53 grade) (350 kg/m³) was used in the concrete mix to prevent shrinkage. Also, class F fly ash (10 % of the mass of cement) was included in the concrete mix to increase the fines and ensure better durability. The specific gravity of cement and fly ash used in the current research are 3.15 and 2.2, respectively. The coarse aggregate used was SFA with a size of approximately 4 mm to 8 mm (Fig. 1) and a specific gravity of 1.45. SFA has water absorption of 15 %. River sand (specific gravity = 2.6) was used as fine aggregate.

Natural coarse aggregates (10 mm) of normal density with a specific gravity of 2.60 were used. Potable water from a local source is used for casting. An effective concrete slump was achieved by using a high-range poly-carboxylate ether-based water reducer. This study uses two types of synthetic fibres, macro fibres and micro fibres. Concrete's crack resistance and ductility are improved by macro fibres, which are bi-component structural fibres. Macro fibres have a rough and hard shell to facilitate bonding with concrete and provide high tensile strength. In micro-fibres, a fibrillated interlinked structure resists micro/shrinkage cracks. The use of synthetic fibres is a desirable alternative to steel fibres in concrete members, because of their resistance to corrosion, residual strengths and chemical stability which can be achieved with lesser weight. Synthetic fibres are economical and produce good post-cracking behaviour [3]. Both types of fibres are shown in Fig. 2, and their properties are listed in Table 1. The macro-fibre dosages of 0.4 % and 0.6 % with a constant micro-fibre dosage of 0.02 % were added. Steel rebar of 10 mm was used as longitudinal reinforcement in concrete.

3.2. Specimen details

Four HCS specimens of 3400 mm length × 600 mm width × 150 mm height were cast. The diameter of the hollow core was kept as 106 mm. The primary reinforcement (steel rebar) is placed in the tension zone with a clear cover of 25 mm. A cross-section view of the HCS is shown in Fig. 3. Specimens without fibres are referred to as control specimens (PO00-HCS). HCS specimens reinforced with fibres are labelled PO04-
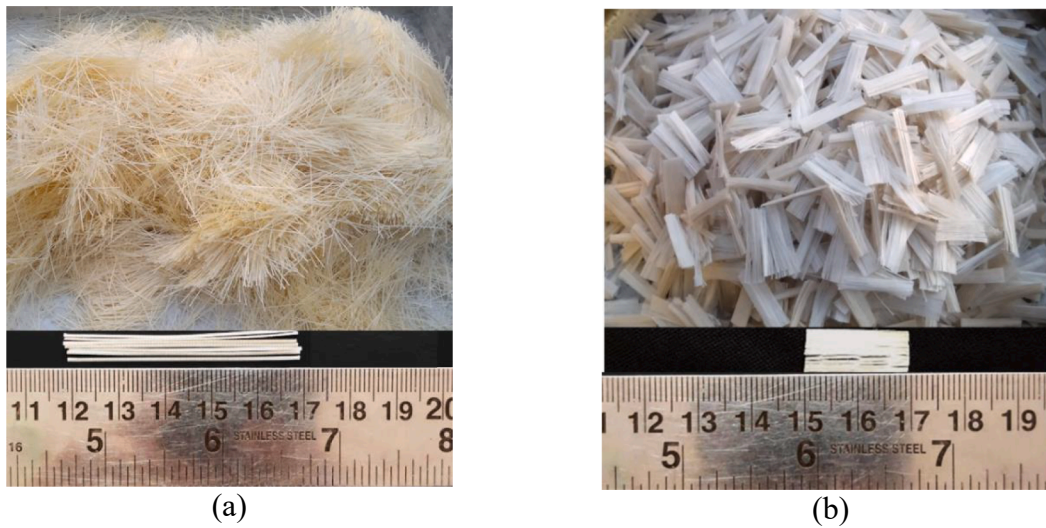
Fig. 2. Fibres: (a) Macro synthetic fibres (b) Micro synthetic fibres.

Table 1
Properties of fibres and reinforcing steel [3].

Parameters	Macro-synthetic fibre	Micro-synthetic fibre	Reinforcing Steel
Shape	Structural fibre	Fibrillated fibre	–
Diameter	0.5 mm	0.08 mm	10 mm
Length	50 mm	19 mm	3500 mm
Specific Gravity	0.91	0.91	7.85
Modulus of Elasticity	10 GPa	4.9 GPa	196 GPa
Tensile Strength	618 MPa	400 MPa	550 MPa

Fig. 3. Cross section of HCS.

HCS and PO06-HCS according to the volume of fibres in the specimen. The specimen nomenclature refers to PO, 04, 06 as polyolefin fibres, 0.4 % and 0.6 % of volume fraction, respectively. In addition to HCS with SLWAC, a conventional concrete HCS with natural coarse aggregate (NCA) was cast for comparison. Natural coarse aggregates of normal density were substituted for sintered fly ash aggregates in NCA concrete mixtures without altering other parameters. The HCS constructed with

natural coarse aggregate are referred to as NCA-HCS in this study.

In NCA concrete, 10 mm natural coarse aggregates with a specific gravity of 2.60 were used. Additionally, three concrete cubes of size 150 mm × 150 mm × 150 mm were cast for every individual mix to find the compressive strength. PO00, PO04, PO06 and NCA specimens had average 28-day cube compressive strengths of 40 MPa, 42 MPa, 46 MPa and 45 MPa, respectively. The optimised concrete mix design is given in Table 2. More details on material characterisation can be found in the previous papers of authors [3,6].

3.3. Mould preparation and casting

Steel moulds with a thickness of 10 mm were used in this study. The moulds have four hollows diameter of 106 mm at both edges. Five small holes of 11 mm diameter were kept at the bottom zone of hollow plates to accommodate steel rebars (Fe 550 grade) of a diameter of 10 mm. Two strain gauges were attached to rebars at the mid-span. Hollow cores were created by inserting water-resistant paper tubes into the hollows of the formwork. The paper tubes had an outer diameter of 104 mm and a thickness of 3 mm.

Cement, sand, and SFA are dry mixed for 2 min in a tilting drum mixer to create a homogeneous mixture. Subsequently, 50 % of the water was collected and blended for two to three minutes. Lastly, the remaining water was added with the superplasticizer. Mixing continued for an additional 3 to 5 min. Fibres were added slowly during mixing to ensure uniform distribution and to prevent agglomeration. For the preparation of specimens, the concrete was poured into the moulds after thorough mixing. First, the bottom layer was cast. Subsequently, the paper tubes were inserted into the holes after wrapping thoroughly with plastic film. The casting of the top layer was done, followed by thorough vibration. After 24 h, the specimens were demoulded, water-cured for 28 days and stacked in a queue for testing. The whole procedure of
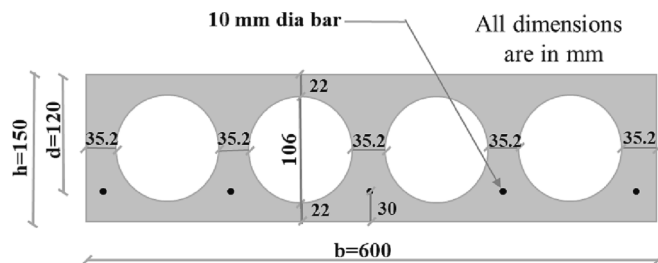
Table 2
Optimized concrete mix proportions.

Mix	C	FA	S	SFA	NCA	W	SP	Macro Fibres	Micro Fibres	W/B	Mean C.S (Cube)	S.D
	(Kg/m³)									0.3	(MPa)	
PO00-HCS	350	35	520	800	0	115	0.3	0	0		40	0.5
PO04-HCS							0.8	3.68	0.184		42	1.5
PO06-HCS							1.0	5.52	0.184		46	1.5
NCA-HCS				0	1450		0.3	0	0		45	1

Note: C = Cement, FA = Fly ash, S = Sand, SFA = Sintered fly ash aggregate, NCA = Natural coarse aggregate, W = Water, W/B = Water to binder ratio, SP = Superplasticizer, C. S = Compressive strength, S.D = Standard deviation.
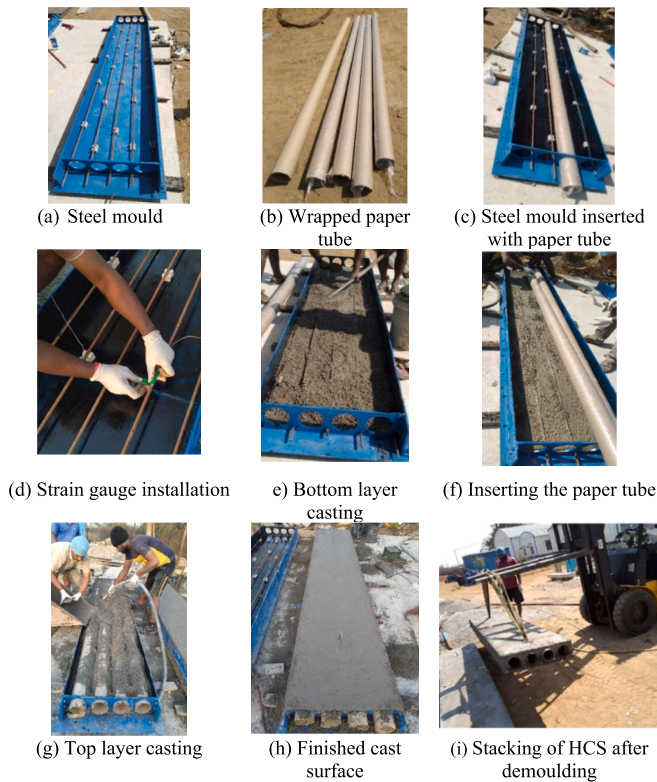
(a) Steel mould

(b) Wrapped paper tube

(c) Steel mould inserted with paper tube

(d) Strain gauge installation

e) Bottom layer casting

(f) Inserting the paper tube

(g) Top layer casting

(h) Finished cast surface

(i) Stacking of HCS after demoulding
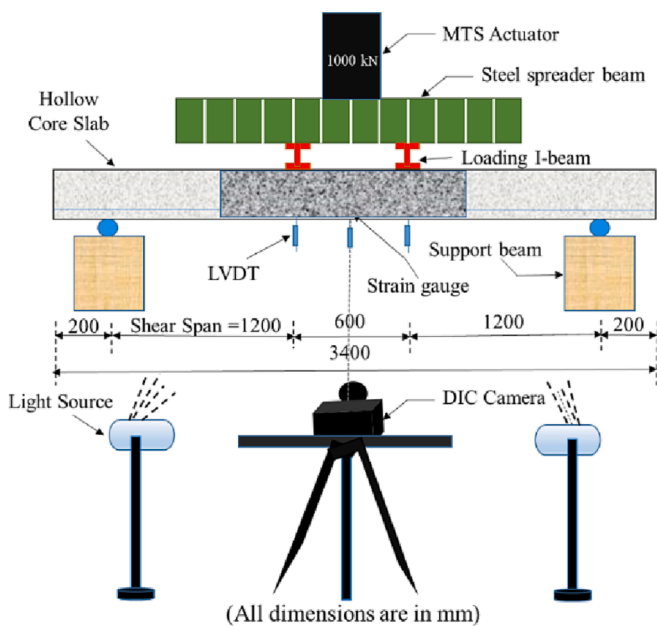
Fig. 4. Casting process of HCS.

Fig. 5. Schematic representation of the experimental setup.

casting is shown in Fig. 4.

3.4. Test setup and instrumentation

To understand the pure flexural behaviour, four HCS specimens were tested under four-point bending. The test setup is schematically shown in Fig. 5, and the actual experimental test setup is presented in Fig. 6. A hydraulic actuator was used to test specimens under displacement control. Each HCS specimen was subjected to the same testing procedure

and load application method.

The load from the actuator was transmitted to the HCS specimen by a rigid longitudinal beam having web stiffeners called spreader beam. Loads from the spreader beam were transmitted to the HCS utilizing two transverse I-beams. High-strength cement mortar grout was applied between the slab surface and spreader I-beams to ensure proper smoothness and avoid surface irregularity. The specimens were pre-loaded before applying the actual loading to ensure that the instruments were operating properly. A pre-load of 3 kN was applied until the displacements stabilised to remove any slack in the system. After that, a monotonic loading was applied in displacement control mode at a rate of 0.03 mm/s. A linear variable displacement transducer (LVDT) of 200 mm stroke was placed at the mid-span of the HCS specimen to measure the mid-span deflection. Strain gauges of 10 mm in gauge length were installed during the casting to measure the strains of the steel rebars corresponding to the mid-span.

Two LVDTs of 50 mm stroke were arranged at the soffit level of the HCS to record the deflection at the loading points. The applied load was measured automatically from the MTS load cell. All these measuring equipment, such as LVDTs and strain gauges, were connected to the data acquisition system (DAQ) for continuous data acquisition.

4. Experimental results and discussion

4.1. Load vs deflection behaviour

All the specimens are tested at an a/d ratio of 10. The load–deflection behaviour of the specimens is shown in Fig. 7. The load–deflection behaviour can be categorised into three different stages: pre-cracking regime, post-cracking regime, and after yielding of the longitudinal bar. In the pre-cracking regime, the load resistance is observed to increase linearly with applied displacement until the cracking of the concrete on the tension face of the slabs. The second stage of the curve starts after flexural cracking and continues up to the yielding of longitudinal rebar. Here, the load resistance increases with a reduced stiffness compared to the pre-cracking regime. The final stage is from yielding of rebar to failure of the specimen. The crack propagation and failure mode type define the strength degradation and level of ductility in the slab element. A comparison of the behaviour of the normal density and lightweight hollow core elements (NCA-HCS, PO00-HCS, PO04-HCS, and PO06-HCS) is presented in Fig. 7 (e). All the tested specimens showed identical behaviour. Compared to normal density HCS specimens, though the ultimate strength was the same, all the lightweight HCS specimens exhibited a marginal reduction in pre-cracking stiffness. Adding fibres did not alter the peak load but increased the post-cracking stiffness marginally. Moreover, adding fibres significantly increased the deflection at the ultimate load and the energy absorption capacity. Specimen with fibres (PO04-HCS and PO06-HCS) has shown more strain energy absorption than control specimens (PO00-HCS and NCA-HCS).

In specimen NCA-HCS (Fig. 7(a)), the initial cracking occurred at a load of 9.3 kN and a deflection of 1.9 mm. After cracking, the specimen experienced a reduction in stiffness. However, before reaching the peak load, the rebar started to yield at a load of 43 kN, corresponding to a deflection of 29 mm. The NCA-HCS reached a peak load of 45.6 kN at the deflection of 70 mm. Finally, the specimen failed due to crushing concrete at a load of 45.2 kN, corresponding to a deflection of 110 mm. The PO00-HCS (Fig. 7(b)), PO04-HCS (Fig. 7(c)), and PO06-HCS (Fig. 7(d)) specimens followed the same trend as exhibited by NCA-HCS. The PO00-HCS, PO04-HCS, and PO06-HCS experienced initial flexure cracking at a load of 10.7 kN, 10.4 kN, and 12.2 kN with the corresponding deflection of 4.1 mm, 4.6 mm, and 3.5 mm, respectively (Fig. 7(f)). The peak loads for the PO00-HCS, PO04-HCS, and PO06-HCS specimens were nearly 44 kN and corresponding deflections in the range of 100 mm. All the tested HCS specimens exhibited under-reinforced behaviour, and the longitudinal rebars yielded before reaching the peak load. The PO00-HCS specimen failed at a load of 43.8 kN corresponding to the
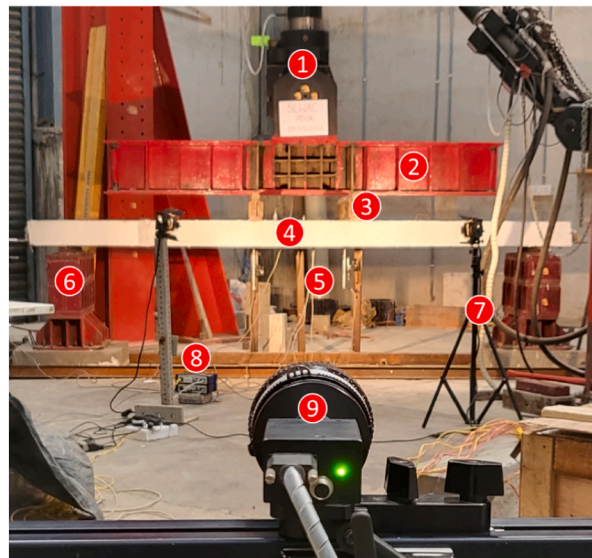
Note: 1-MTS Actuator, 2-Steel Spreader Beam, 3-Loading I-Beam, 4- Hollow Core Slab, 5-LVDT, 6- Support Beam, 7- Light Source, 8- DAQ, 9- DIC Camera

Fig. 6. Experimental test setup.

displacement of 112 mm. FR-LWHCS (PO04-HCS and PO06-HCS) specimens did not fail even after reaching 140 mm deflection. Testing was stopped at 140 mm prior to failure due to limitations in stroke capacity. PO04-HCS and PO06-HCS specimens reached a maximum load of 42.4 kN and 44.5 kN, respectively.

The deflections of all the tested specimens (NCA-HCS, PO00-HCS, PO04-HCS, and PO06-HCS) under design service loads were 5 mm, 3.8 mm, 4.4 mm, and 2.7 mm, respectively. The calculation of service load is shown in Appendix A. The results show that the deflection of FR-LWHCS at service loads for 0.6 % fibre dosage is lesser than that of the HCS made of normal density concrete. The loads at a short-term deflection limit of 10 mm (Span/350) [40] are about 15 kN for all the HCS specimens. This comparison indicates that FR-LWHCS has a similar load carrying capacity at serviceability limit to HCS made of normal density concrete.

The summary of test results is presented in Table 3. The strain energy absorption of all HCS specimens was calculated by estimating the area under the load–deflection curve. Despite the same a/d ratio used in testing, all specimens had different fibre dosages. The strain energy absorption capacity of NCA-HCS was found to be 4535 Joule. The strain energy absorption of PO00-HCS was approximately 10 % lesser than NCA-HCS. However, the strain energy absorption capacities of PO04-HCS and PO06-HCS were about 12 % higher than NCA-HCS. Since the testing of two specimens was aborted at a mid-span deflection of 140 mm due to the limitation in stroke capacity, energy absorption presented considers a maximum deflection of 140 mm. Otherwise, strain energy absorption would be substantially higher than the values presented. Due to the crack arresting mechanism of FR-LWHCS specimens, the deflection at ultimate load is higher than control specimens.

4.2. Load vs strain behaviour

The strain variations during testing were measured with strain gauges installed on the rebars at mid-length at the maximum bending moment location. The load vs strain curve is shown in Fig. 8. The initial change in slope is due to the formation of flexural cracks. At higher loads, the change in slope is due to the yielding of longitudinal rebar. Strain values up to 10000 μm/m were recorded. It is worth noting that the stresses in the rebars were negligible until cracking. Post-cracking,

the strains increased significantly as expected. At 2750 μm/m, the rebar reached its yielding strength. The fibre reinforced HCS specimen has a lower strain at a particular load than the control specimen. The strain decreases with an increase in fibre dosages which shows the influence of fibres in resisting load. In all the HCS specimens, the steel rebar yielded before it reached its peak load.
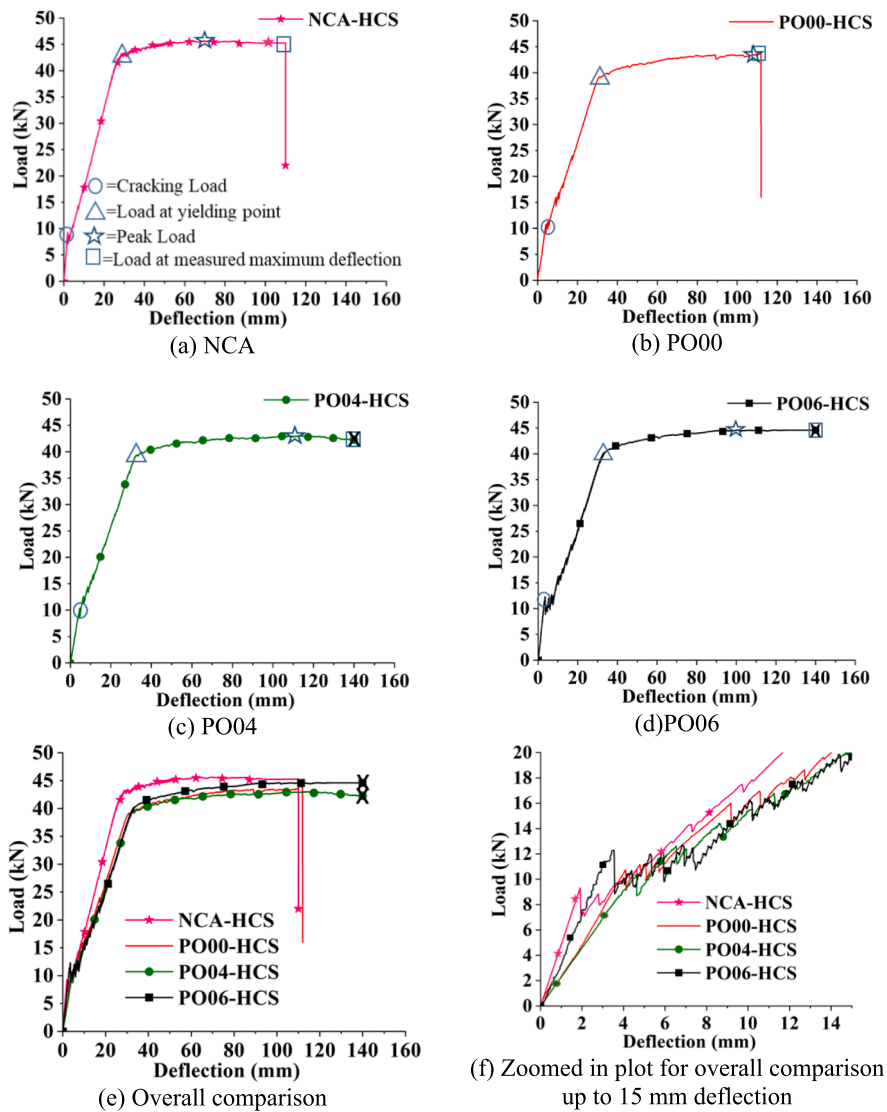
4.3. Crack distribution and failure modes

For all the HCS specimens, the number of cracks initially increased continuously as the load gradually increased. It also contributed to an increase in crack width. Cracks stabilized due to bond transfer limits at the rebar interface and concrete at higher loads. Due to this, the number of cracks and distribution did not change at the later stage of loading. All the HCS specimens failed in flexure mode. When fibres were introduced to LWHCS, the number of cracks steadily increased and the distance between cracks reduced, as seen in Fig. 9. Thus, the fibres play an essential role in bridging cracks in HCS specimens and deformability of LWHCS. Fig. 9 depicts the failure modes.

After cracking in specimens without fibre (NCA-HCS and PO00-HCS), cracks propagated faster and failed at lower displacement than fibre-reinforced specimens (PO04-HCS and PO06-HCS). The number of cracks in fibre reinforced HCS specimens were significantly more than in the control HCS specimens. Cracks were more distributed, and the distance between cracks was shorter in fibre-reinforced specimens. Due to the low strength of SFA, the crack penetrates through aggregate in lightweight concrete. Therefore, the cracks develop faster when compared to normal-density concrete. The crack passes around the aggregate in the HCS made of normal density concrete. Due to this, cracks were meandering in NCA-HCS as compared to PO00-HCS. All HCS specimens had longitudinal fractures at the bottom. Fig. 10 depicts the crack pattern at the bottom of PO04- HCS. All the other HCS specimens exhibited a similar failing pattern on the tension side (bottom).

4.4. Fibre distribution

After testing FR-LWHCS, the fibre distribution on the cracked surface was examined. The orientation of synthetic fibres on the failure surface is shown in Fig. 11. It depicts more or less uniform distribution of fibres

(a) NCA

(b) PO00

(c) PO04

(d)PO06

(e) Overall comparison

(f) Zoomed in plot for overall comparison up to 15 mm deflection

Note 1: 'X' signifies the testing has been stopped at 140 mm deflection in PO04-HCS and PO06-HCS.

Fig. 7. Load vs deflection behaviour.

Table 3
Summary of test results.

Parameters	NCA-HCS	PO00-HCS	PO04-HCS	PO06-HCS
a/d	10.0	10.0	10.0	10.0
Cracking load (kN)	9.3	10.7	10.4	12.2
Deflection at cracking load (mm)	1.9	4.1	4.6	3.5
Peak load (kN)	45.6	43.9	43.0	44.6
Deflection at peak load(mm)	70.0	110.0	114.4	101.0
Load at measured maximum deflection (kN)	45.2	43.8	42.2	44.5
Measured maximum deflection (mm)	110.0	112.0	140.0*	140.0*
Cracking moment (kN-m)	5.6	6.4	6.2	7.3
Peak moment (kN-m)	27.3	26.3	25.8	26.7
Strain energy absorption (Joule)	4535.2	4105.0	5233.0*	5404.0*
Mode of failure	Flexure	Flexure	Flexure	Flexure

*Test aborted at 140 mm due to stroke limitation of the actuator.

along the width of the section. The failure surface was investigated to identify the active participation of the number of fibres in the fracture process and the failure mechanisms. Fibre pull-out and rupture of fibres demonstrate the contributions of fibres to load resistance. This study uses a maximum fibre dosage of 0.6 % to avoid balling effect and segregation. The number of fibres per area considered across the width of the failure section is shown in Fig. 12.

4.5. DIC analysis

Digital image correlation (DIC) is a technique for evaluating the full-field strain and displacement of HCS specimens. DIC aids in tracking and analysing the crack generation and propagation. The surface of the HCS specimen was randomly speckled, after a coating with acrylic-based white paint. The DIC technique involves tracking speckles in deformed images by comparing the patterns of speckles to a reference image. DIC employs a high-quality camera (1024x768 pixels) and a light source as part of the setup. The photos were captured at a frame rate of one per second and saved on a computer for post-processing. Vic-2D [41] software was used to analyse it afterwards. Before loading, a reference
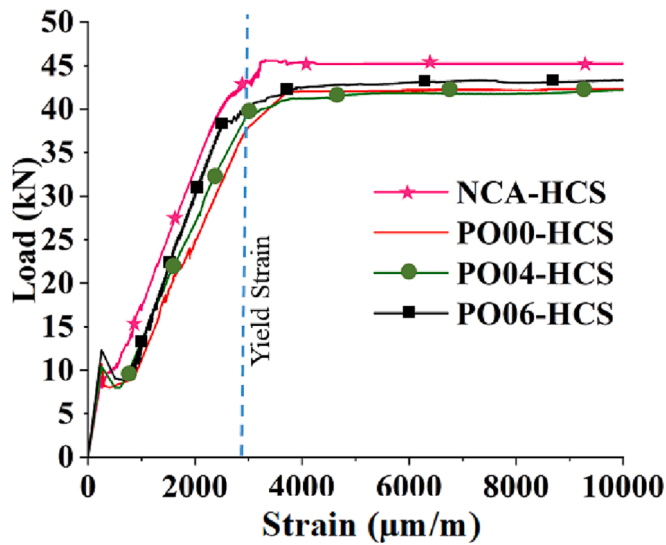
Fig. 8. Load vs strain of rebar.

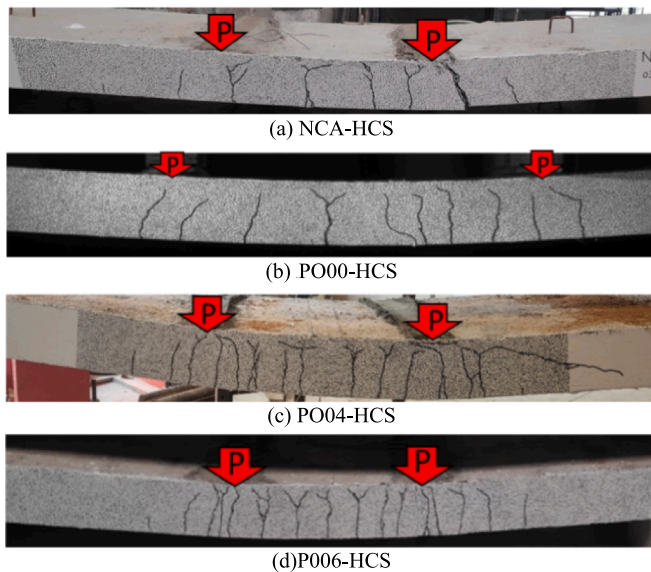(a) NCA-HCS

(b) PO00-HCS

(c) PO04-HCS

(d)P006-HCS

Fig. 9. Failure modes of HCS.

image (calibration image) was obtained, which corresponds to the initial location of speckles. The accuracy of DIC results depends upon the size of the speckles and subset size. Following a thorough review of the literature, a subset size of 35 and a step size of 5 were considered [42].

Researchers have proved that DIC analysis successfully agrees with experimental results in predicting the structural behaviour of concrete [43,44].

4.5.1. Validation of DIC results with experimental results

A comparison was made between the load–deflection behaviour of the four HCS specimens utilising DIC analysis and LVDT (at mid-span) measurements. DIC analysis results agreed with the LVDT measurements, as shown in Fig. 13. Only PO06-HCS is represented to avoid data duplication.

4.5.2. Strain contours

DIC analysis compared the strain distribution at selected loading points (cracking, yielding, peak, ultimate) to understand the failure progression. The strain distribution was examined to assess the contribution of fibres to resist the propagation of the crack. The crack was initiated and propagated from the bottom and slowly progressed towards the top of the HCS. At initial loads (up to cracking), the strain contours of FR-LWHCS and control HCS specimens followed the same pattern. The previous observation indicates that fibres do not play a significant role in the load carrying mechanism before cracking of the concrete. In HCS, the jump in strain contours represents the existence of a crack in that region. The strain contours of all the HCS are interpreted in Fig. 14.

4.5.3. Load vs crack width

Crack width is an essential parameter for the serviceability assessment. Fig. 15a illustrates the relationship between load and crack width measured using DIC analysis. The crack width is measured at the reinforcement level at each specimen. At lower load levels, the crack width is zero for HCS specimens up to 9.3 kN, 10.7 kN, 10.4 kN and 12.2 kN for NCA-HCS, PO00-HCS, PO04-HCS and PO06-HCS specimens, respectively. The crack width starts to increase with the increase in applied load. At any load level, the crack widths of FR-LWHCS specimens are smaller than control specimens. Thus, FR-LWHCS specimens are more efficient in controlling the crack propagation than the control LWHCS specimen and normal density HCS. PO06-HCS have the lowest crack width, followed by PO04-HCS, PO00-HCS and NCA-HCS at a particular load level. NCA-HCS and PO00-HCS had crack widths of 0.15 mm and 0.1 mm at service load, respectively. However, PO04-HCS and PO06-HCS have insignificant crack widths (Fig. 15b). Increasing the number of fibres can be beneficial for controlling crack width and the serviceability performance of LWHCS.

5. Numerical studies

Finite element models of HCS specimens were created using the commercially available finite element software package. The HCS models were created and loaded at an a/d ratio of 10. In FE modelling, the boundary conditions and loading conditions of the HCS adopted in
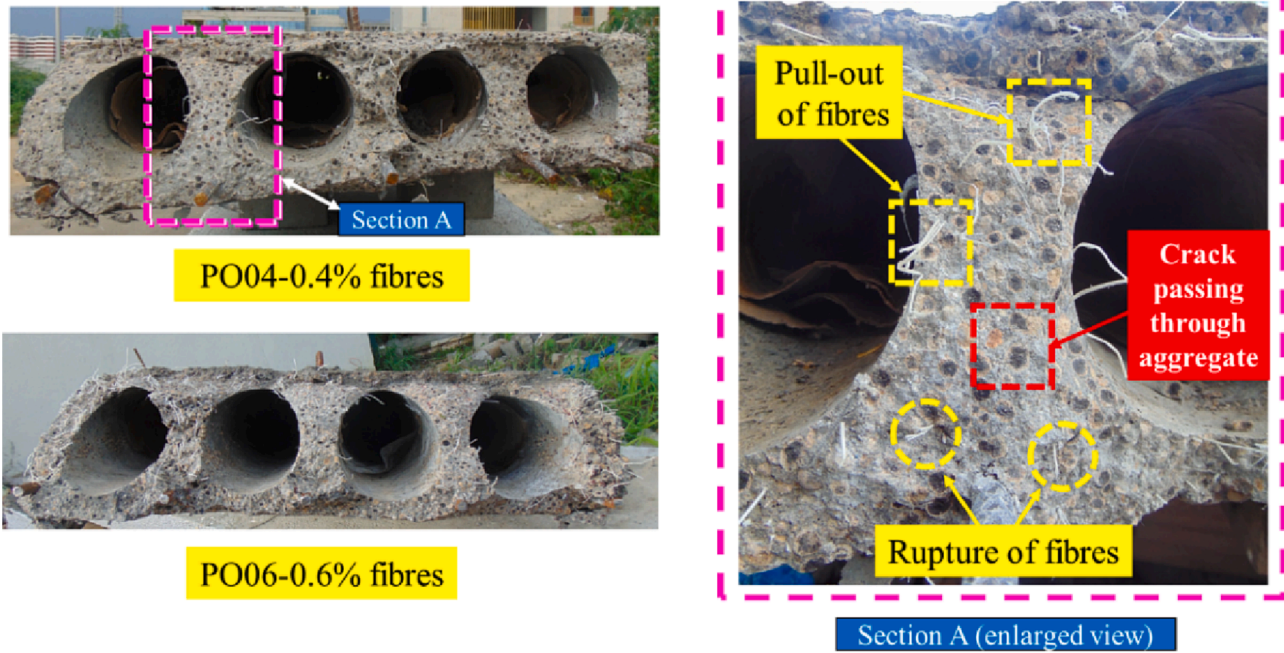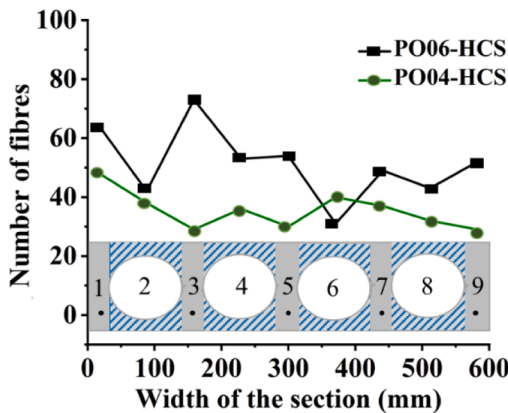

Fig. 10. Crack pattern on the tension side of FR-LWHCS (PO04).

Fig. 11. Orientation of fibres at failure surface.

Note: HCS is divided into nine zones and fibres are counted.

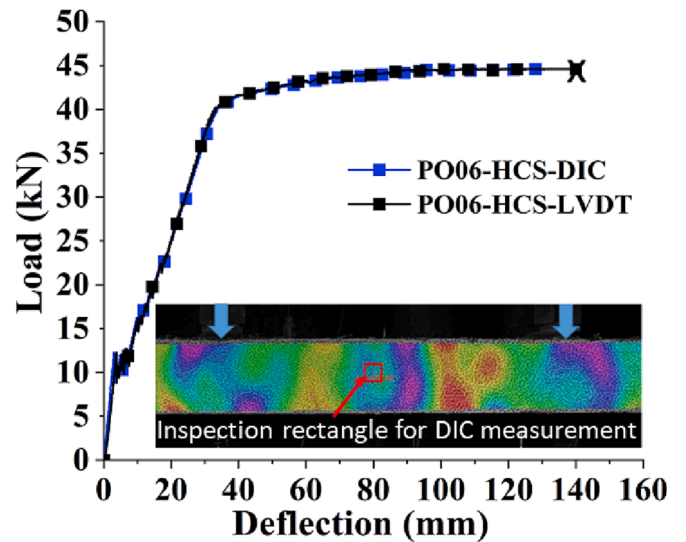**Fig. 12.** Fibre distribution across failure section.

Fig. 13. Load vs Deflection comparison between LVDT and DIC.

the experiments were closely represented. The concrete damage plasticity (CDP) model, which can accurately describe the behaviour of quasi-brittle materials like concrete, is used to model concrete damage. CDP model was derived from the concepts proposed by Lubliner et al. [45] and Lee and Fenves [46]. The CDP model for concrete is based on both plasticity and continuum-based damage mechanics. CPD model accounts for the two primary failure mechanisms of concrete crushing in compression and cracking in tension. Concrete was modelled using C3D8R, a 3D, eight-node element developed to predict concrete's response in ABAQUS [47]. Similarly, a truss element (T3D2) was used to model rebars. The truss elements can withstand compression and tension but are not capable of resisting the moment. Explicit model analysis was used to prevent the convergence problem. The stress–strain behaviour of concrete consists of elastic and plastic characteristics. The total strain of concrete is characterized by a combination of elastic and plastic strains. Plasticity and damage responses of concrete are demonstrated by the nonlinear portion of the stress–strain response.

Several assumptions were made in the model regarding the mate-

rials, such as homogeneous and rate-independent materials. The effects of temperature and moisture were not considered. It does not consider time-dependent characteristics like creep and relaxation as well. Compressive stress–strain curves (Fig. 16) for input are taken from the authors' previous research [3], and tensile stress–strain curves (Fig. 17) obtained by using inverse analysis results are taken from the authors' previous paper [6]. The prediction of the tensile stress–strain curve for FR-SLWAC with different volumes of synthetic fibres has been made with the help of stress- crack width model by performing inverse analysis. The stress-crack width model is established using the load-*CMOD* (Crack mouth opening displacement) curve obtained from the fracture test. Stress at a particular crack width ($\sigma_{(w)}$) is calculated by using Eq. (1)

$$\sigma_{(w)} = [f_t - f_{pk}e^{-w_{pk}^2 c_{pk}}]e^{-32} + 1.5w^2 e^{-dw} + f_{pk}e^{-(w-w_{pk})^2 c_{pk}} \qquad (1)$$

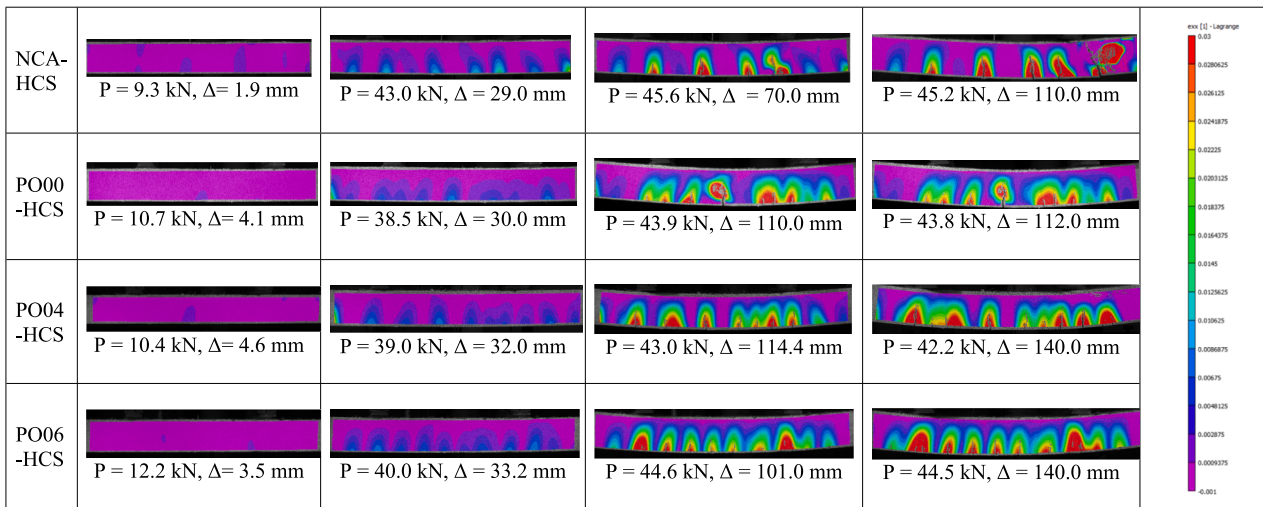The crack width at second peak stress (w_{pk}), the stress at its second

NCA-HCS	P = 9.3 kN, Δ= 1.9 mm	P = 43.0 kN, Δ = 29.0 mm	P = 45.6 kN, Δ = 70.0 mm	P = 45.2 kN, Δ = 110.0 mm
PO00-HCS	P = 10.7 kN, Δ= 4.1 mm	P = 38.5 kN, Δ = 30.0 mm	P = 43.9 kN, Δ = 110.0 mm	P = 43.8 kN, Δ = 112.0 mm
PO04-HCS	P = 10.4 kN, Δ= 4.6 mm	P = 39.0 kN, Δ = 32.0 mm	P = 43.0 kN, Δ = 114.4 mm	P = 42.2 kN, Δ = 140.0 mm
PO06-HCS	P = 12.2 kN, Δ= 3.5 mm	P = 40.0 kN, Δ = 33.2 mm	P = 44.6 kN, Δ = 101.0 mm	P = 44.5 kN, Δ = 140.0 mm

Fig. 14. Strain contours at different key points of the load–deflection curve.
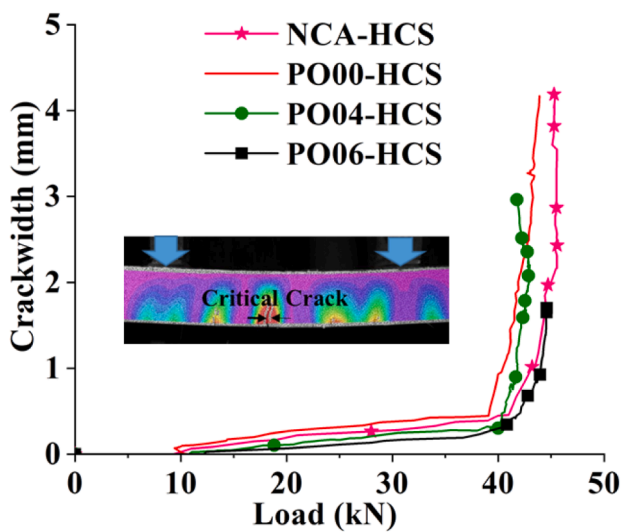
Fig. 15a. Variation in crack width with increase in load.
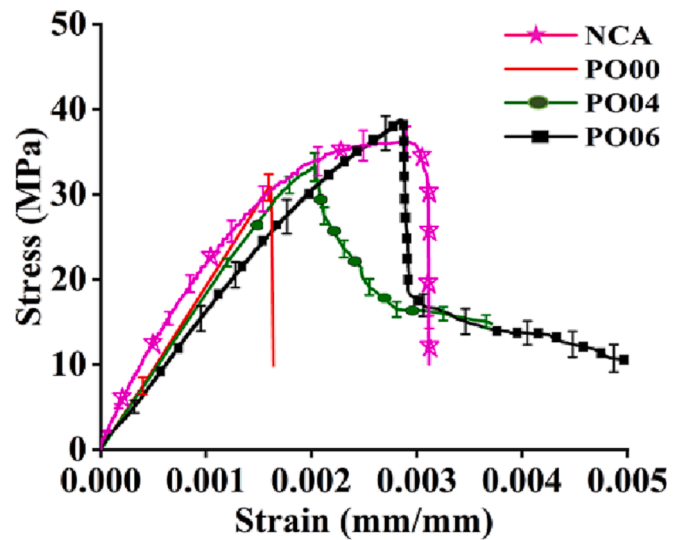

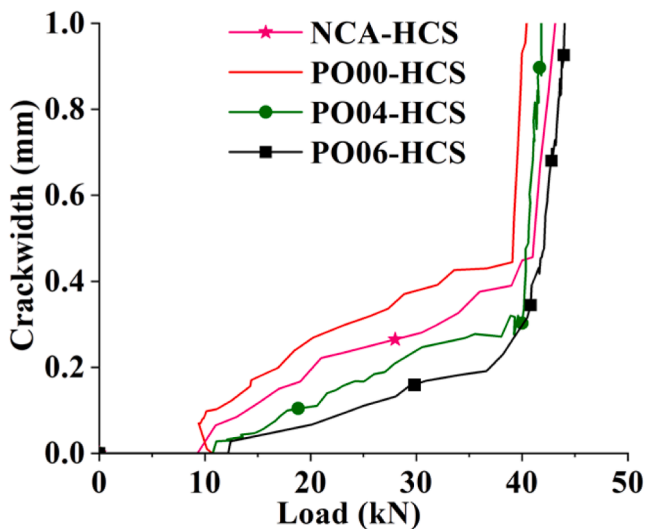**Fig. 16.** Stress–strain curve for compression.

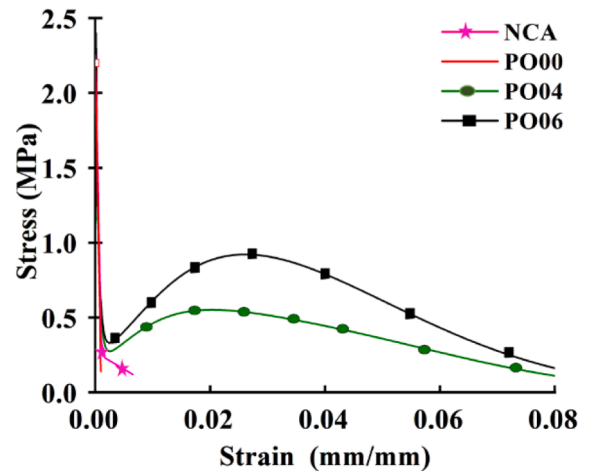**Fig. 15b.** Variation in crack width up to 1 mm with increase in load.

Fig. 17. Stress–strain curve for tension.

Table 4
Plasticity constants for concrete.

ψ	ε	$\frac{f_{bo}}{f_{co}}$	μ	K
40	0.1	1.16	0.0005	0.667

peak (f_{pk}) and Curvature coefficient for the exponential heap (C_{pk}) can be calculated using Eqs. (2), (3) and (4), respectively. The volume fraction of fibres and modulus of elasticity of fibres can be used to estimate the above-mentioned key parameters.

$$w_{pk} = 2 \times 10^{-5} E_f^2 V_f - 5 \times 10^{-5} E_f^2 - 0.4 V_f + 2.5 \qquad (2)$$

$$f_{pk} = 1.5 V_f^2 - 1.1 V_f + 0.5 + 0.0002263 E_f^{2.8} \qquad (3)$$

$$C_{pk} = 1.108 \times 10^{-6} E_f^2 V_f - 5.485 \times 10^{-4} E_f^1 + 0.1654 + (V_f - 0.75)/25 \qquad (4)$$

As shown in Eq. (5), the strain corresponding to each crack width could be estimated using the pre-cracking strain, crack width, and hinge width.

$$\varepsilon = [(w/s) + f_t/(E_c)] \qquad (5)$$

w = Crack width, s = hinge width, f_t = Uniaxial tensile strength, E_f = Modulus of elasticity of fibre (10 GPa), V_f = Fibre volume fraction, d = Constant = 0.8/ V_f, ε = Strain, f_{ck} = Compressive strength of concrete, E_c = Modulus of elasticity of concrete.

Different parameters assumed for the CDP model are dilation angle (ψ), eccentricity (ε), the ratio of biaxial yield stress to uniaxial yield stress ($\frac{f_{bo}}{f_{co}}$), viscosity parameter (μ) and the coefficient to obtain the shape of the deviatory cross-section (K) are considered for fibre-reinforced lightweight concrete from Al-Thairy et al. [35] given in Table 4.

It is possible to model progressive material damage using the CDP model because the damage is an essential factor which influences concrete non-linearity. It is a scalar damage variable varying from 0 to 1. The damage variable in compression (d_c) and damage variable in tension (d_t) is determined as per Eqs. (5)–(6) based on Huang and Liew [48]. The damage variables in concrete are influenced by various factors such as stress, strain and modulus of elasticity.

$$d_c = 1 - \frac{\sigma_c + n_c f'_c}{[E_c (n_c \sigma_c / E_c + \varepsilon_c)]} \qquad (5)$$

$$d_f = 1 - \frac{\sigma_t + n_t f_t}{[E_c (n_t \sigma_t / E_c + \varepsilon_t)]} \qquad (6)$$

where,

σ_c = Compressive stress.
σ_t = Tensile stress.
f'_c = Cylinder compressive strength of concrete.
E_c = Modulus of elasticity of concrete.
ε_c = Concrete strain in compression.
ε_t = Concrete strain in tension.
n_c, n_t = 2 (compression and tension stress- strains responses constant).

An optimal mesh size of 30 mm was used in the analysis for the HCS after performing mesh sensitivity analysis. Same mesh size was assigned to all the elements to ensure that each material has the same node as another. This model uses structured meshes.

The boundary conditions in FEM were carefully matched with those in the actual test. Nodes at the top surface were displaced downward at a distance from support nodes for an a/d ratio of 10. As a displacement-controlled load application, a downward deflection of the slab was applied to the entire line of nodes until failure. The displacement was
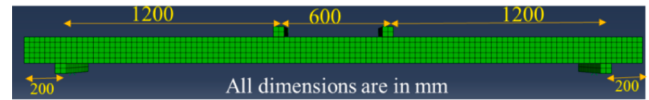
(a) Test Configuration
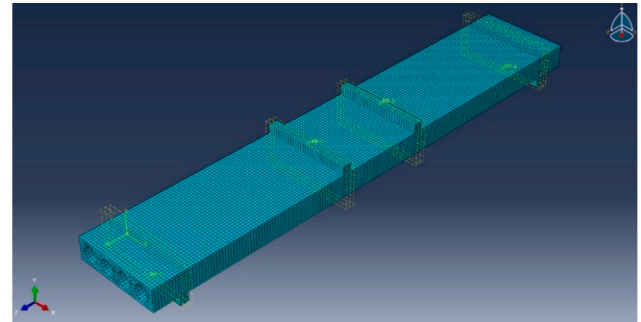
(b) Mesh

Fig. 18. FEM Simulation in ABAQUS.

increased in small steps after cracking to avoid convergence difficulties. The FEM simulation is shown in Fig. 18, which consists of the test configuration (Fig. 18(a)) and mesh (Fig. 18(b)).

5.1. Comparison of load–deflection behaviour

To ensure the accuracy of the FE model, the predictions were compared with the experimental results of the tested HCS. Fig. 19 shows the load–deflection behaviour of all HCS specimens acquired from the experiment and FE model. The developed model closely estimates load–deflection behaviour results from the experimental data.

5.2. Summary of experimental and FEM results

The numerical findings of the FEM simulation imply that the behaviour of lightweight hollow core slabs with and without synthetic fibres can be predicted using the FE programme ABAQUS. Salient FE results are compared with test data in Table 5. The variation between peak load obtained from test results and FE results are within 5 % for all the specimens, indicating the modelling approach's adequacy. The cracking load obtained from FE was more than the experimental value in NCA-HCS. However, the cracking load was similar in the remaining three specimens. Similarly, the strain energy absorptions (area under the load–deflection curve) of all HCS specimens were compared between test results and FE results. The difference in strain energy absorptions derived from test results and FE and experimental results were within 5 %.

5.3. Comparison of failure modes

A comparison of crack patterns in HCS based on FE models and the experimental test is shown in Fig. 20. It was observed that the main cracks formed at the middle third of the slab (flexural cracks). The FE model closely predicted the crack distributions and failure modes.

6. Comparison with current design code

The design of hollow core slabs is governed by the *ACI* 318-19 [49]. Cracking load and peak load from experiments have been compared with theoretical calculations based on codal provisions (Table 5). When compared to experimental findings, it was found that *ACI* 318-19 [49] under predicts the cracking load and peak load. The cracking load of NCA-HCS, PO00-HCS, PO04-HCS and PO06-HCS was found to be 9.2 kN, 8.6 kN, 8.8 kN, 9.5 kN respectively. The cracking loads are
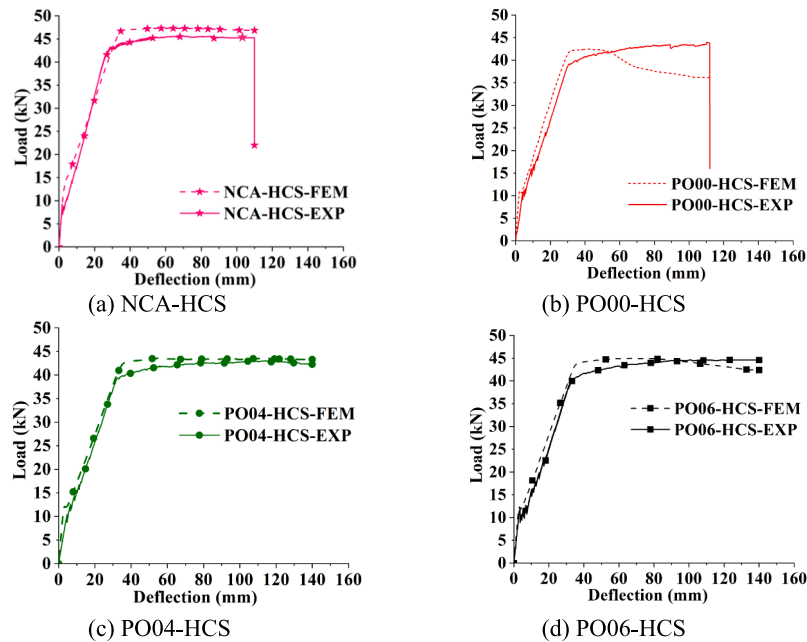
Fig. 19. Load vs Deflection curve (Experimental vs FEM).

Table 5
Summary of experimental, theoretical and FEM results.

Specimen ID	CL_{EXP}(kN)	CL_{FEM}(kN)	CL_{ACI}(kN)	PL_{EXP}(kN)	PL_{FEM}(kN)	PL_{ACI}(kN)	SE_{EXP}(Joule)	SE_{FEM}(Joule)	$\frac{CL_{EXP}}{CL_{FEM}}$	$\frac{CL_{EXP}}{CL_{ACI}}$	$\frac{PL_{EXP}}{PL_{FEM}}$	$\frac{PL_{EXP}}{PL_{ACI}}$	$\frac{SE_{EXP}}{SE_{FEM}}$
NCA-HCS	9.3	13.5	9.2	45.6	47.3	36.6	4535.2	4357.3	0.69	1.01	0.96	1.24	1.04
PO00-HCS	10.7	10.9	8.6	43.9	42.4	35.8	4105.0	3938.8	0.98	1.24	1.03	1.22	1.04
PO04-HCS	10.4	11.7	8.8	43.0	43.5	36.3	5233.0	5418.5	0.88	1.18	0.99	1.17	0.96
PO06-HCS	12.2	12.1	9.5	44.6	44.9	37.3	5404.0	5515.0	1.01	1.28	0.99	1.20	0.98

Note: CL_{EXP} = Experimental cracking load, CL_{FEM} = Predicted cracking load using FEM, CL_{ACI} = Theoretical cracking load using ACI 318-19 [49] codal provision, PL_{ACI} = Theoretical peak load using ACI 318-19 [49] codal provision, PL_{EXP} = Experimental peak load, PL_{EXP} = Predicted peak load using FEM, SE_{EXP} = Experimental strain energy absorption, SE_{FEM} = Predicted strain energy absorption using FEM.
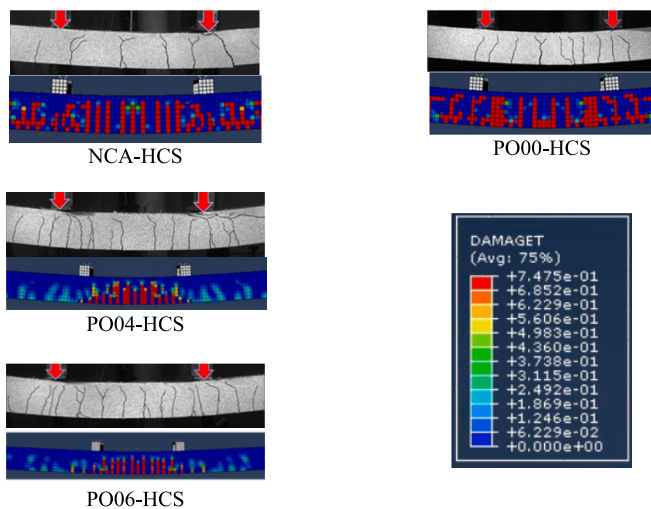

Fig. 20. Comparison of failure modes (Experimental vs FEM).

approximately same in normal concrete and 20 to 30 % less in lightweight concrete. The peak load of NCA-HCS, PO00-HCS, PO04-HCS and PO06-HCS was found to be 36.6 kN, 35.8.0 kN, 36.3.4 kN, 37.3 kN respectively which is approximately 20 % less than the peak load from the experimental results. The theoretical formulae for calculation are given in Appendix B.

7. Summary and conclusions

An innovative and sustainable lightweight fibre reinforced hollow core slabs were developed and tested in this study. The effect of macro synthetic fibre reinforcement on the flexural behaviour of FR-LWHCS was evaluated. Four slabs were tested with varying fibre content at an a/d ratio of 10. The following conclusion can be obtained based on the limited results presented in this study.

I. Using lightweight concrete in precast HCS led to a reduction in weight of 25 %. Fibre-reinforced lightweight HCS achieved peak and ultimate loads close to HCS made of normal density concrete under flexure.

II. The behaviour of the fibre-reinforced hollow core slabs demonstrates that adding the fibres resist crack growth and enhance strain energy absorption.

III. Load- deflection curve of all the HCS specimens followed the same trend. Limited results show that a minimum fibre dose of 0.4 % should be included in lightweight HCS to provide adequate strain energy absorption without significantly compromising strength and stiffness. Future work should focus on further optimizing the fibre combination and dosages.
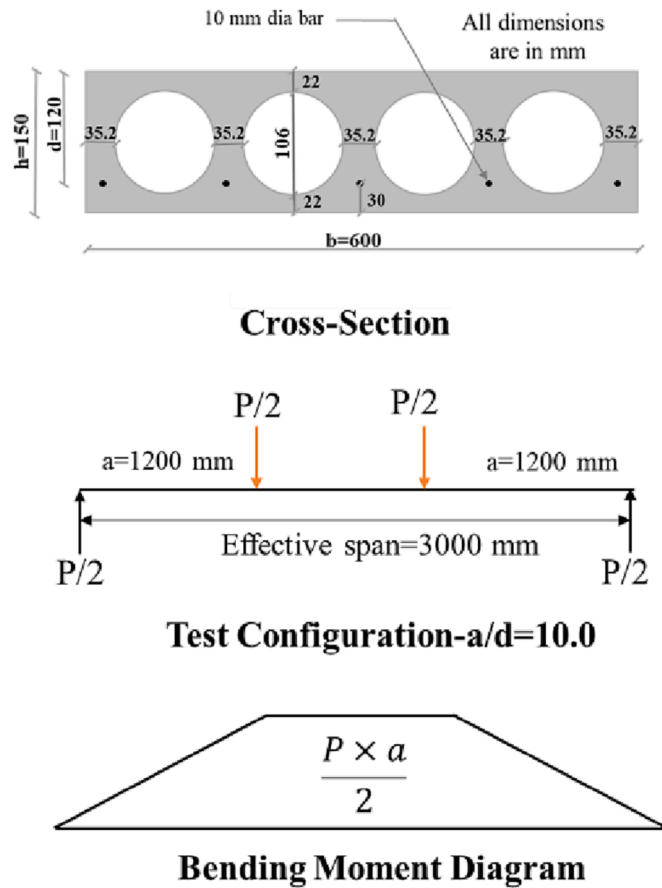
Fig. 21. Cross-section, Test configuration and Bending moment diagram of HCS.

measurement using DIC showed that FR-LWHCS has less crack width at service loads than HCS made of normal density concrete. The deflection of FR-LWHCS at service loads for 0.6 % fibre dosage was also lesser than that of the HCS made of normal density concrete.

V. The cracking load and peak load predictions using *ACI* code are conservative in nature.

VI. Establishing proper constitutive models of lightweight concrete is essential for accurate FE modelling. The load–deflection behaviour and failure modes from FE modelling compared well with test results.

CRediT authorship contribution statement

Sumit Sahoo: Conceptualization, Methodology, Investigation, Validation, Writing – original draft. **Chetharajupalli Veerendar:** Methodology, Investigation, Software, Validation, Formal analysis. **S. Suriya Prakash:** Data curation, Supervision, Writing – review & editing.

Declaration of Competing Interest

The authors declare that they have no known competing financial interests or personal relationships that could have appeared to influence the work reported in this paper.

Data availability

Data will be made available on request.

IV. The DIC technique accurately traced the crack progression, strains at different locations, and failure modes. Crack width

Appendix A

Calculation of design service load:

Cross-sectional area of HCS $= (0.6m \times 0.15m) - \left(4 \times \frac{\pi}{4} \times 0.106^2 m^2\right) = 0.055m^2$

For PO00-HCS, PO04-HCS and PO06-HCS the density of concrete is taken as $1800 Kg/m^3$.

Self-weight of the HCS $= \left(0.055m^2 \times 1800 Kg/m^3 \times 9.81 m/s^2\right) = 0.97 kN/m$

Typical super imposed load in residential applications $= \left(1.5 kN/m^2 \times 0.6m\right) = 0.9 kN/m$

Weight of screed flooring $= \left(0.075m/m \times 25 kN/m^2 \times 0.6m\right) = 1.125 kN/m$

Typical live loads in residential applications $= \left(3 kN/m^2 \times 0.6m\right) = 1.80 kN/m$ [40].

Total service load (w) $= (0.97 + 0.9 + 1.125 + 1.8) kN/m = 4.8 kN/m$

Bending moment (demand) in service $= \frac{wl^2}{8} = \frac{4.55 \frac{kN}{m} \times (3.0m)^2}{8} = 5.4 kNm$

Design service load from four-point bending test configuration (P):

$$\frac{P}{2} \times 1.2 = 5.4 kNm; P = 9.0 kN$$

It is calculated that PO00-HCS, PO04-HCS, and PO06-HCS have a service load of 9 kN each.

For NCA-HCS, the density of concrete $2400 Kg/m^3$ is used in the calculation keeping all other parameters the same and the design service load (P) is estimated to be 9.6 kN.

The cross-section, test configuration and bending moment diagram of HCS is shown in Fig. 21. An a/d ratio of 10 is used in the calculation to conservatively estimate the service loads.

Appendix B

Flexural capacity calculation using current design code *ACI* 318-19 [49].

For reinforced concrete, prestressing components have been discarded from the formulas given in *ACI* 318-19 [49].

Flexural moment Capacity = $M_n = A_{ps}F_{ps}\left(d_p - \frac{a}{2}\right)$

$$a = \frac{A_{ps}F_{ps}}{0.85f_c' b_w}$$

Cracking moment $= M_{cr} = \frac{I}{y_b}\left(0.62\lambda\sqrt{f_c'}\right)$ Where,

A_{ps} = Area of steel rebar = 392 mm^2.

F_{ps} = Stress at nominal strength = 550 MPa.

d_p = Effective depth of HCS = 120 mm.

f_c' = Cylinder compressive strength = 35 MPa (NCA), 30 MPa (PO00), 33 MPa (PO04), 38 MPa (PO06).

b_w = net web width of the slab = 176 mm.

I = Moment of Inertia about the centroid of the section = 146×10^6 mm^4.

y_b = Distance from the centroidal axis of the gross section to the tensile force = 74 mm.

λ = Modification factor for lightweight concrete = 0.75.

References

[1] H.P. Satpathy, S.K. Patel, A.N. Nayak, Development of sustainable lightweight concrete using fly ash cenosphere and sintered fly ash aggregate, Constr. Build. Mater. 202 (2019) 636–655, https://doi.org/10.1016/j.conbuildmat.2019.01.034.

[2] X. Liu, T. Wu, Y. Liu, Stress-strain relationship for plain and fibre-reinforced lightweight aggregate concrete, Constr. Build. Mater. 225 (2019) 256–272, https://doi.org/10.1016/j.conbuildmat.2019.07.135.

[3] S. Sahoo, A.K. Selvaraju, S. Suriya Prakash, Mechanical characterization of structural lightweight aggregate concrete made with sintered fly ash aggregates and synthetic fibres, Cem. Concr. Compos. 113 (2020) 103712.

[4] M.S. Nadesan, P. Dinakar, Structural concrete using sintered flyash lightweight aggregate: A review, Constr. Build. Mater. 154 (2017) 928–944, https://doi.org/10.1016/j.conbuildmat.2017.08.005.

[5] L. Domagała, Durability of structural lightweight concrete with sintered fly ash aggregate, Materials (Basel). 13 (2020) 1–20, https://doi.org/10.3390/ma13204565.

[6] S. Sahoo, C. Lakavath, S.S. Prakash, Experimental and analytical studies on fracture behavior of fiber-reinforced structural lightweight aggregate concrete, J. Mater. Civ. Eng. 33 (2021) 04021074, https://doi.org/10.1061/(asce)mt.1943-5533.0003680.

[7] M. Di Prisco, M. Colombo, D. Dozio, Fibre-reinforced concrete in fib Model Code, Principles, models and test validation, Struct. Concr. 14 (2013) (2010) 342–361, https://doi.org/10.1002/suco.201300021.

[8] J. Gao, W. Sun, K. Morino, Mechanical properties of steel fiber-reinforced, high-strength, lightweight concrete, Cem. Concr. Compos. 19 (1997) 307–313, https://doi.org/10.1016/S0958-9465(97)00023-1.

[9] M.A. Rasheed S.S. Prakash Experimental study on compression behavior of fiber-reinforced cellular concrete stack-bonded masonry prisms ACI Mater. J. 115 2018 149 160 https://doi.org/10.14359/51701241.

[10] A. Enfedaque, M. Alberti, J. Gálvez, Influence of fiber distribution and orientation in the fracture behavior of polyolefin fiber-reinforced concrete, Materials (Basel) 12 (2) (2019) 220.

[11] N. Buratti, C. Mazzotti, M. Savoia, Post-cracking behaviour of steel and macro-synthetic fibre-reinforced concretes, Constr. Build. Mater. 25 (2011) 2713–2722, https://doi.org/10.1016/j.conbuildmat.2010.12.022.

[12] M.A. Rasheed, S.S. Prakash, Behavior of hybrid-synthetic fiber reinforced cellular lightweight concrete under uniaxial tension – Experimental and analytical studies, Constr. Build. Mater. 162 (2018) 857–870, https://doi.org/10.1016/j.conbuildmat.2017.12.095.

[13] A. Bhosale, M.A. Rasheed, S.S. Prakash, G. Raju, A study on the efficiency of steel vs. synthetic vs. hybrid fibers on fracture behavior of concrete in flexure using acoustic emission, Constr. Build. Mater. 199 (2019) 256–268, https://doi.org/10.1016/j.conbuildmat.2018.12.011.

[14] A.A. Al-Azzawi B.M. Abdul Al-Aziz Behavior of reinforced lightweight aggregate concrete hollow-core slabs Comput. Concr. 21 2018 117 126 https://doi.org/10.12989/cac.2018.21.2.117.

[15] I.A. Al-Shaarbaf, A.A. Al-Azzawi, R. Abdulsattar, A state of the art review on hollow core slabs, ARPN J. Eng. Appl. Sci. 13 (2018) 3240–3245.

[16] L.V. Prakashan, J. George, J.B. Edayadiyil, J.M. George, Experimental study on the flexural behavior of hollow core concrete slabs, Appl. Mech. Mater. 857 (2016) 107–112, https://doi.org/10.4028/www.scientific.net/amm.857.107.

[17] C.-H. Lee, I. Mansouri, E. Kim, K.-S. Hwang, W.-T. Woo, Flexural strength of one-way composite steel deck slabs voided by circular paper tubes, J. Struct. Eng. 145 (2019) 04018246, https://doi.org/10.1061/(asce)st.1943-541x.0002259.

[18] F.H. Naser, A. Hameed, N. Al, M.K. Dhahir, Effect of using different types of reinforcement on the flexural behavior of ferrocement hollow core slabs embedding PVC pipes, Ain Shams Eng. J. 12 (2021) 303–315, https://doi.org/10.1016/j.asej.2020.06.003.

[19] L.-H. Khali, T. Elshafiey, M. Hussein, A. Baraghith, A. Etman, Shear behavior of innovated composite hollow core slabs, Int. Conf. Adv. Struct. Geotech. Eng. (2019) 13.

[20] A.L. Materazzi M. Breccolotti I. Venanzi Fire performance of HPLWC hollow core slabs Proc. Fourth Int. Work. Struct. Fire SiF'06 2006 May, Aveiro, Port.

[21] S. Li, C. Song, Mechanical performance test and analysis of prestressed lightweight aggregate concrete hollow slab, Adv. Struct. Eng. 22 (2019) 1830–1844, https://doi.org/10.1177/1369433219825998.

[22] Y. Nassif Sabr H. Khalaf Jarallah H. Issa AbdulKareem Improving Shear Strength of Thick Hollow Core Slabs By Using Lightweight High Strength Concrete Produced From Recycled Crushed Clay Brick and Iron Powder Waste J. Eng Sustain. Dev. 23 2019 128 146 https://doi.org/10.31272/jeasd.23.6.10.

[23] N.G. Wariyatno, Y. Haryanto, G.H. Sudibyo, Flexural behavior of precast hollow core slab using PVC pipe and styrofoam with different reinforcement, Procedia Eng. 171 (2017) 909–916, https://doi.org/10.1016/j.proeng.2017.01.388.

[24] P. Kankeri S.K.S. Pachalla N. Thammishetti S.S. Prakash Behavior Of Structural Macrosynthetic Fiber-Reinforced Precast, Prestressed Hollow-Core Slabs at Different Flexure-to-Shear Ratios PCI J. 64 2019 76 91 https://doi.org/10.15554/pcij64.3-01.

[25] A.K. Azad, I.Y. Hakeem, Flexural behavior of hybrid hollow-core slab built with ultra high performance concrete faces, Mater. Struct. Constr. 49 (2016) 3801–3813, https://doi.org/10.1617/s11527-015-0755-7.

[26] G. Kani, How safe are our large concrete beams, ACI J, Proc, 1967.

[27] C. Lakavath, S.S. Joshi, S.S. Prakash, Investigation of the effect of steel fibers on the shear crack-opening and crack-slip behavior of prestressed concrete beams using digital image correlation, Eng. Struct. 193 (2019) 28–42, https://doi.org/10.1016/j.engstruct.2019.05.030.

[28] E. Cuenca, P. Serna, Failure modes and shear design of prestressed hollow core slabs made of fiber-reinforced concrete, Compos. Part B Eng. 45 (2013) 952–964, https://doi.org/10.1016/j.compositesb.2012.06.005.

[29] K. Paine, Increasing the shear strength and ductility of prestressed hollow core slabs using metal fibres, 4th Int Symp. Noteworthy Dev. Prestress. Precast. Singapore (1997) 25–26.

[30] C.H. Peaston K.S. Elliott K.A. Paine Steel fiber reinforcement for extruded prestressed hollow core slabs Am. Concr. Institute, ACI Spec. Publ. SP-182 1999 87 107 https://doi.org/10.14359/5523.

[31] A. Pisanty, The shear strength of extruded hollow-core slabs, Mater. Struct. 25 (1992) 224–230, https://doi.org/10.1007/BF02473067.

[32] H.T. Li, A.J. Deeks, L.X. Liu, D.S. Huang, X.Z. Su, Moment transfer factors for column-supported cast-in-situ hollow core slabs, J. Zhejiang Univ. Sci. A. 13 (2012) 165–173, https://doi.org/10.1631/jzus.A1100170.

[33] E. Brunesi, D. Bolognini, R. Nascimbene, Evaluation of the shear capacity of precast-prestressed hollow core slabs: numerical and experimental comparisons, Mater. Struct. 48 (2015) 1503–1521, https://doi.org/10.1617/s11527-014-0250-6.

[34] L. Jin, X.-A. Jiang, H. Xia, F. Chen, X. Du, Size effect in shear failure of lightweight concrete beams wrapped with CFRP without stirrups: Influence of fiber ratio, Compos. Part B Eng. 199 (2020) 108257.

[35] H. Al-Thairy, S.K. Al-Jasmi, Numerical investigation on the behavior of reinforced lightweight concrete beams at elevated temperature, Iran. J. Sci. Technol. - Trans Civ. Eng. 45 (2021) 2397–2412, https://doi.org/10.1007/s40996-021-00580-4.

[36] X. Liu, Y. Liu, T. Wu, H. Wei, Bond-slip properties between lightweight aggregate concrete and rebar, Constr. Build. Mater. 255 (2020), 119355, https://doi.org/10.1016/j.conbuildmat.2020.119355.

[37] S.K.S. Pachalla S.S. Prakash Load Resistance and Failure Modes of Hollow-Core Slabs with Openings: A Finite Element Analysis PCI J. 63 2018 25 40 https://doi.org/10.15554/pcij63.4-03.

[38] V. Albero, A. Espinós, E. Serra, M.L. Romero, A. Hospitaler, Numerical study on the flexural behaviour of slim-floor beams with hollow core slabs at elevated temperature, Eng. Struct. 180 (2019) 561–573, https://doi.org/10.1016/j.engstruct.2018.11.061.

[39] X. Li, G. Wu, M. Shafiq Popal, J. Jiang, Experimental and numerical study of hollow core slabs strengthened with mounted steel bars and prestressed steel wire ropes, Constr. Build. Mater. 188 (2018) 456–469, https://doi.org/10.1016/j.conbuildmat.2018.08.073.

[40] IS 456, Plain Concrete and Reinforced, Bur. Indian Stand. Dehli. (2000) 1–114.

[41] Correlated Solutions, Vic-2D, (2009) 59.

[42] G. Crammond, S.W. Boyd, J.M. Dulieu-barton, Speckle pattern quality assessment for digital image correlation, Opt. Lasers Eng. 51 (2013) 1368–1378, https://doi.org/10.1016/j.optlaseng.2013.03.014.

[43] S.S. Joshi, N. Thammishetti, S.S. Prakash, Efficiency of steel and macro-synthetic structural fibers on the flexure-shear behaviour of prestressed concrete beams, Eng. Struct. 171 (2018) 47–55, https://doi.org/10.1016/j.engstruct.2018.05.067.

[44] A. Dev, M. Chellapandian, S.S. Prakash, Effect of macrosynthetic and hybrid fibers on shear behavior of concrete beams reinforced with GFRP bars, J. Bridg. Eng. 25 (2020) 04020031, https://doi.org/10.1061/(asce)be.1943-5592.0001557.

[45] J. Lubliner, J. Oliver, S. Oller, E. Onate, A plastic-damage model, Int. J. Solids Struct. 25 (1989) 299–326.

[46] J. Lee, G.L. Fenves, Plastic-damage model for cyclic loading of concrete structures, J. Eng. Mech. 124 (1998) 892–900, https://doi.org/10.1061/(asce)0733-9399(1998)124:8(892).

[47] A. Gui, T. Reference, Abaqus GUI Toolkit Reference Manual Abaqus 6.11 GUI Toolkit Reference Manual, Dassault Syst. Simulia Corp. Provid. RI, USA. (2011).

[48] Z. Huang, J.Y.R. Liew, Nonlinear finite element modelling and parametric study of curved steel-concrete-steel double skin composite panels infilled with ultra-lightweight cement composite, Constr. Build. Mater. 95 (2015) 922–938, https://doi.org/10.1016/j.conbuildmat.2015.07.134.

[49] ACI, 318-19 Building Code Requirements for Structural Concrete and Commentary, American Concrete Institute, 2019. https://doi.org/10.14359/51716937.